Neurochemistry International 125 (2019) 163–174

Contents lists available at ScienceDirect

Neurochemistry International

journal homepage: www.elsevier.com/locate/neuint

Correlative study using structural MRI and super-resolution microscopy to detect structural alterations induced by long-term optogenetic stimulation of striatal medium spiny neurons

Yoshifumi Abe[a,*], Yuji Komaki[b,c], Fumiko Seki[b,c], Shinsuke Shibata[b,d], Hideyuki Okano[b,d,e], Kenji F. Tanaka[a]

[a] Department of Neuropsychiatry, Keio University School of Medicine, Japan
[b] Department of Physiology, Keio University School of Medicine, Japan
[c] Live Imaging Center, Central Institute for Experimental Animals, Japan
[d] Electron Microscope Laboratory, Keio University School of Medicine, Japan
[e] Laboratory for Marmoset Neural Architecture, RIKEN Center for Brain Science, Japan

ARTICLE INFO

Keywords:
DTI
Optogenetics
Medium spiny neuron
Axon
Myelin

ABSTRACT

Striatal medium spiny neurons (MSNs) control motor function. Hyper- or hypo-activity of MSNs coincides with basal ganglia-related movement disorders. Based on the assumption that lasting alterations in neuronal activity lead to structural changes in the brain, understanding these structural alterations may be used to infer MSN functional abnormalities. To infer MSN function from structural data, understanding how long-lasting alterations in MSN activity affect brain morphology is essential. To address this, we utilized a simplified model of functional induction by stimulating MSNs expressing channelrhodopsin 2 (ChR2). Subsequent structural alterations which induced long-term activity changes in these MSNs were investigated in the striatal pathway and its associated regions by diffusion tensor imaging (DTI) and histological assessment with super-resolution microscopy. DTI detected changes in the striatum, substantia nigra, and motor cortex. Histological assessment found a reduction in the diameter of myelinated cortical axons as well as MSN dendrites and axons. The structural changes showed a high correlation between DTI parameters and histological data. These results demonstrated that long-term neural activation in the MSNs alters the diameter of MSN and cortical neurons fibers. This study provides a tool for understanding the causal relationship between functional and structural alterations.

1. Introduction

Striatal medium spiny neurons (MSNs) and their circuits have an important role in controlling motor function (Hikosaka et al., 2000). Many studies have reported that changes in MSN activity coincide with basal ganglia-related movement disorders (e.g. Parkinson's disease and dystonia) (Nambu, 2005; Bronfeld and Bar-Gad, 2011; Nambu et al., 2011; Wichmann and Dostrovsky, 2011). These reports suggest that hyper- or hypo-activity changes in MSNs induce neuronal morphological alterations in the axons, dendrites, and myelin. Based on the assumption that long-lasting alterations in neuronal activity induce structural changes in the brain, a clear understanding of these structural alterations may be used to infer functional abnormalities in MSNs. However, the mechanism by which long-lasting neural activation of MSNs affects morphological changes in the MSNs themselves and their circuits remains unknown. For this reason, it is difficult to speculate about the relationship between pathophysiological changes associated with basal ganglia-related movement disorders and the underlying structural changes.

Diffusion tensor imaging (DTI), a structural MRI technique, can be used to detect structural changes in the brain, in particular, morphological alterations in axons and myelin throughout the brain. DTI visualizes the diffusion of water molecules, which is greatly influenced by tissue microstructure (Basser et al., 1994a, 1994b; Le Bihan et al., 2001; Mori and Zhang, 2006). Fractional anisotropy (FA), mean diffusivity (MD), radial diffusivity (RD), and axial diffusivity (AD) are computed DTI values which reflect microstructural changes (e.g., in myelin and fibers). These DTI values have been widely applied to the estimation of white matter structural changes in myelin content and neural fibers (Feldman et al., 2010; Thomason and Thompson, 2011; Yano et al.,

* Corresponding author. 35 Shinanomachi, Shinjuku, Tokyo, 160-8582, Japan.
E-mail address: abeyoshihumi@gmail.com (Y. Abe).

https://doi.org/10.1016/j.neuint.2019.02.017
Received 6 September 2018; Received in revised form 20 February 2019; Accepted 22 February 2019
Available online 27 February 2019
0197-0186/

2018). The FA value is a summary measure of microstructural integrity. The RD value reflects the structural status of myelin as well as axons. The AD value reflects the pathological status of axonal fibers. The MD value reflects cellular status such as cellularity, edema, and necrosis, although MD is less sensitive to the status of myelin and axonal fibers than FA, RD, and AD (Sagi et al., 2012; Yano et al., 2018).

To address how long-lasting neural activation of MSNs affects morphological changes in the MSNs themselves and their circuits, we conducted a proof-of-concept study using mice that express channelrhodopsin-2 (ChR2) in their MSNs. Optogenetic MSN stimulation enables long-term upregulation of specific neuronal populations. We employed FA, RD, and AD as the DTI parameters for comprehensive visualization of the structural alterations induced by long-term optogenetic stimulation of the MSNs. In addition, post-hoc histological assessment was used to determine the precise structural changes using a structured illumination microscope with super-resolution microscopy (SIM-SRM). Once the affected brain regions are identified based on changes in DTI parameters, the macroscopic structural alterations described by DTI can be confirmed using a microscopic histological approach. This combination of optogenetics-mediated long-term neuronal activation and structural surveys using DTI and histological assessment permits the causal relationship between functional and structural changes to be determined. Here, through the combination of a DTI study followed by histological assessment with SIM-SRM, we show that long-term upregulation of neural activity in the striatal MSNs induces structural alterations in the striatal pathway and the associated cortex.

2. Materials & methods

2.1. Animals

MSN-ChR2 mice (Pde10a2-tTA::tetO-ChR2 (C128S)-YFP double-transgenic mice) were obtained by crossing the *Pde10a2*-tTA mice (Sano et al., 2008) and tetO-ChR2-YFP mice (Tanaka et al., 2012) (See Fig. 1D). To sufficiently express the ChR2 protein in the targeted cell population, we took advantage of an improved tetracycline-controllable gene induction system (KENGE-tet system) (Tanaka et al., 2012). A total of 8 (8-week-old) male MSN-ChR2 mice were used for DTI assessment and histological analysis by SIM-SRM and EM (see Supplemental Table 1).

Animal experiments were approved by the Keio University Animal Experiment Committee in compliance with Keio University Animal Experimental Regulations (approval number: 12035-5). All animals were housed in temperature- and humidity-controlled rooms on a 12 h light/dark cycle (lights on at 8:00 a.m.).

2.2. Animal surgery and optogenetic stimulation

Mice were anesthetized with a ketamine-xylazine mixture (100 mg/kg and 10 mg/kg, respectively, i.p.) and fixed in a stereotaxic frame (Narishige, Tokyo, Japan). A 470 nm LED (TeleLP-c, 3.5 mm × 3.5 mm, BRC Bioresearch center, Ltd, Nagoya, Tokyo) with an LED battery (TeleR, 3 g, BRC Bioresearch center, Ltd, Nagoya, Tokyo) was placed on the right side of the skull above the striatum (+1.7 mm lateral, + 0.5 mm anterior from the bregma; Fig. 1B). After surgery, the mice were housed individually and allowed a 7-day recovery period before starting the experiments (Fig. 1E). Optogenetic stimulation (0.5 s/hour, approximately 0.2 mW/mm^2) was then continuously applied in the housing cage for 7 days. Video recording was performed to observe the daily rotation behavior of each mouse and the number of rotations were counted.

Tissue preparation of DTI samples was described previously (Yano et al., 2018). After the 7-day stimulation, each mouse was deeply anesthetized with a ketamine-xylazine mixture then transcardially perfused with 4% (w/v) paraformaldehyde (PFA) which was diluted with 0.1 M phosphate-buffer solution (PBS, pH 7.4) and 0.2 mM gadolinium (Magnevist, Bayer Yakuhin, Ltd, Osaka, Japan). Brain tissues were kept within the skulls and were post-fixed overnight with 4% PFA then were immersed in 0.2 mM gadolinium (Magnevist) containing PBS for 1–2 weeks (Fig. 1E). Two brains within their skulls were firmly fixed using fitted sponges in an acrylic tube (21 mm diameter) filled with Fluorinert (Sumitomo 3M Limited, Tokyo, Japan) to minimize the signal intensity attributed to the embedding medium (Dazai et al., 2011).

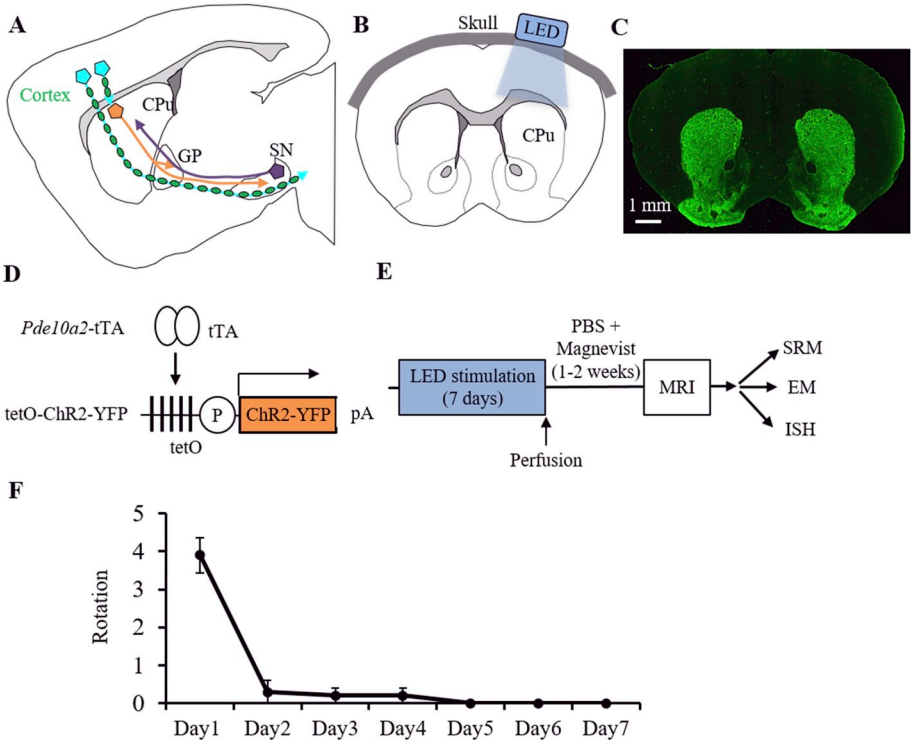

Fig. 1. Experimental design. (A) Schematic diagram of the striatal pathway evaluated in this study. Green neurons represent the cortical myelinated neurons and green ellipses indicate the myelin. The orange neuron represents an MSN (unmyelinated neuron) expressing ChR2. The purple neuron represents a dopamine neuron from the SN. (B) Long-term optogenetic stimulation to the right striatum was performed using an LED placed above the skull. (C) A representative image showing expression of ChR2-YFP (green) in the striatum. (D) Regulation of tTA by the *Pde10a2* promotor activates tetO to express ChR2-YFP protein. (E) Time course of the experimental design. Perfusion was performed 7 days after optogenetic stimulation. MRI (*ex vivo* DTI) was subsequently performed with the isolated brains after permeation of the brain in PBS solution containing Magnevist for 1–2 weeks. Serial brain sections were analyzed by SRM, EM and *in situ* hybridization (ISH). (F) The number of rotation behaviors during the optogenetic stimulations over 7 continuous days are shown (n = 8).

2.3. DTI acquisition

The method for DTI acquisition was described previously (Yano et al., 2018). An *ex vivo* DTI study of mouse brains was performed with a 7 T Biospec 70/16 MRI scanner (Bruker Biospin GmbH; Ettlingen, Germany) equipped with actively shielded gradients at a maximum strength of 700 mT/m and a transmitting/receiving volume coil with an inner diameter of 22 mm. DTI images of two brains were obtained simultaneously. B0 homogeneity was determined using two brains and was ensured using automatic iterative FASTMAP methods (ParaVision 6.01). A 3D DTI-spin echo protocol was used for the acquisition of the DTI images of the whole brain with the following parameters: time of repetition (TR) = 150 ms, time of echo (TE) = 18.8 ms, number averaged = 5, b-value = 1500 s/mm^2, image number with b = 0 s/mm^2 = 4, number of encoding directions of the motion probing gradient (MPG) = 30, diffusion time δ = 3 ms, Δ = 10 ms, maximum gradient strength = 533 mT/m, field of view = 17 × 12 × 19 mm^3, matrix size = 136 × 96 × 152, spatial resolution = 125 × 125 × 125 μm^3, acquisition time = 60 h.

A phantom consisting of saline with 0.2 mM gadolinium (Magnevist) in two cylinders with a diameter (6.3 mm) approximately the same size as a mouse brain were prepared. The two cylinders were firmly fixed using fitted sponges and were put in an acrylic tube filled with Fluorinert. DTI images of the phantom were obtained using the same sequence as the *ex vivo* DTI study. T1-weighted images were obtained using a 2D fast-low angle shot (FLASH) with the following parameters: TR = 300 ms, TE = 5 ms, number averaged = 30, field of view = 17.6 × 17.6 mm^2, matrix size = 220 × 220, slice thickness = 0.9 mm, slice number = 12, spatial resolution = 80 × 80 × 900 μm^3, acquisition time = 15 min.

2.4. DTI analysis

The method for DTI analysis was described previously (Yano et al., 2018). The DTI analysis was performed using DSI studio (http://dsi-studio.labsolver.org/). A diffusion tensor was modeled at each voxel of the DTI image. Scalar anisotropy and diffusivity maps were obtained from the resulting diffusion tensor eigenvalues (λ_1, λ_2, λ_3) which captured the length of the longest, middle, and shortest axes of the ellipsoid. FA, RD, and AD were calculated from the standard formulae (Le Bihan et al., 2001; Alexander et al., 2007):

A region of interest (ROI) was manually set for the ipsilateral and contralateral sides of the whole caudate-putamen (wCPu), dorsal CPu (dCPu), ventral CPu (vCPu), nuclear accumbens (NAc), globus pallidum (GP), ventral pallidum (VP), substantia nigra pars reticula (SNr), motor cortex (M), and somatosensory cortex (SS) corresponding to the averaged b0 image with MRIcron software (http://www.mricro.com/). The dCPu and vCPu were defined by the upper and lower regions of the trisected CPu. The same ROI was used to measure FA, RD, and AD values using MarsBar (MRC Cognition and Brain Sciences Unit, Cambridge, UK) (Fig. 2C).

Tractography was performed using DSI studio (http://dsi-studio.labsolver.org/). Tracks were generated using the FACT algorithm with tracking of the principal eigenvector (e_1) in each voxel. The e_1 associated with the largest eigenvalue (λ_1) was assumed to represent the local coherent fiber orientation. The angle of deflection threshold between contiguous voxels was set at 35°. The threshold of the FA value was set at 0.12. We set two ROIs at the ipsilateral and contralateral dCPu corresponding to the ROIs of Fig. 2C and associated the tract fibers with the ROIs.

2.5. Tissue preparation for histological studies

After the *ex vivo* DTI study, the same fixed brains were cryoprotected in 20% sucrose/phosphate buffered saline (PBS) overnight, frozen, and coronal sections were cut at a thickness of 25 μm on a cryostat. Brain serial sections were used in subsequent immunohistochemistry (IHC), visualized using super-resolution microscopy (SRM), electron microscopy (EM), and *in situ* hybridization (ISH).

2.6. Immunohistochemistry

Serial sections obtained after DTI were incubated in an anti-proteolipid protein (PLP) rat monoclonal antibody (AA3, 1:1 dilution, hybridoma supernatant, a gift from Dr. Kazuhiro Ikenaka at the National Institute for Physiological Sciences, Japan) (Inamura et al., 2012), an anti-GFP goat antibody (1:250; Rockland Immunochemicals Inc., Limerick, PA, USA) to enhance the YFP signal, and an anti-beta 3 tubulin rabbit antibody (1:500; Abcam plc., Cambridge, UK) overnight at room temperature. The sections were then incubated with secondary antibodies conjugated to Alexa Fluor 555 and 647 (1:1000; Invitrogen, Grand Island, NY) for 2 h at RT.

The protocol for mounting tissue from the SIM-SRM was previously described (Mito et al., 2016). Prior to mounting, the concentration of 2,2′-thiodiethanol (TDE) was increased in a stepwise manner (10%, 25%, 50%, and 97% in PBS) to prevent shrinking of the samples by osmotic shock; the samples were incubated in each concentration of TDE for 5 min. Mounting medium (97% TDE, 0.24% DABCO in PBS) was applied to the samples and they were mounted with coverslips (thickness: No.1, Matsunami Glass Ind. Ltd., Osaka, Japan). TDE and DABCO were purchased from Sigma-Aldrich Japan, Tokyo, Japan.

Macro images of the sections were captured using an inverted light microscope (BZ-X710, Keyence, Osaka, Japan). SIM-SRM micro images were obtained using a Zeiss ELYRA 3D-SIM system equipped with an EM-CCD camera. Before obtaining the SIM-SRM images, precise alignment for the different wavelengths of light was performed using mounting solution containing 0.1% Tetraspeck (0.2 μm beads, Thermo Fisher Scientific, MA, USA), to correct for the alignment not coinciding due to unavoidable laser misalignment and optical aberrations at this extremely high-resolution. 14–20 Z-section images were obtained at an interval of 126 nm using a 64 × objective lens. The number of pattern rotations of the structured illumination was adjusted to 3 in the ELYRA system. After obtaining all images, the SIM images were reconstructed and were aligned using the channel alignment data.

2.7. Electron microscopy

The serial sections obtained after DTI were used for EM analysis as described previously (Shibata et al., 2015). Briefly, the sections were dried and fixed at 4 °C with 2.5% glutaraldehyde in 0.1 M phosphate buffer (PB, pH 7.4) for 24 h. Glass slide-mounted sections were washed at 4 °C in 0.1 M PB for 5 min, followed by post-fixation with 1.0% osmium tetroxide for 2 h. Sections were dehydrated through graded (70–100%) ethanol, 100% acetone, with 100% n-butyl glycidyl ether (QY-1), a graded concentration of Epon with QY-1, and embedded in 100% Epon. Polymerization was completed at 60 °C with pure Epon for 72 h. After removing the sections from the glass slides using a 110 °C hot plate, the block with the target area (dCPu) was dissected and fixed on the sectioning stage at 60 °C for 12 h. Then 70 nm ultrathin sections were prepared on copper grids and stained with uranyl acetate and lead citrate for 10 min. The sections were observed using a TEM (JEOL, 1400 plus) and quantitatively analyzed.

2.8. In situ hybridization

The serial sections obtained after DTI were fixed in 4% PFA in PBS for 20 min, followed by two washes with PBS for 5 min, and treated with 40 μg/mL proteinase K (Roche, Japan) for 30 min. The sections were then washed with PBS for 5 min and post-fixed with 4% PFA in PBS for 15 min to inactivate the proteinase K. After washing with PBS for 5 min, the sections were acetylated with 0.25% acetic anhydride. Prehybridization was carried out for 2 h at 60 °C in hybridization buffer containing 50% formamide (Wako, Japan), 50X Denhardt's solution

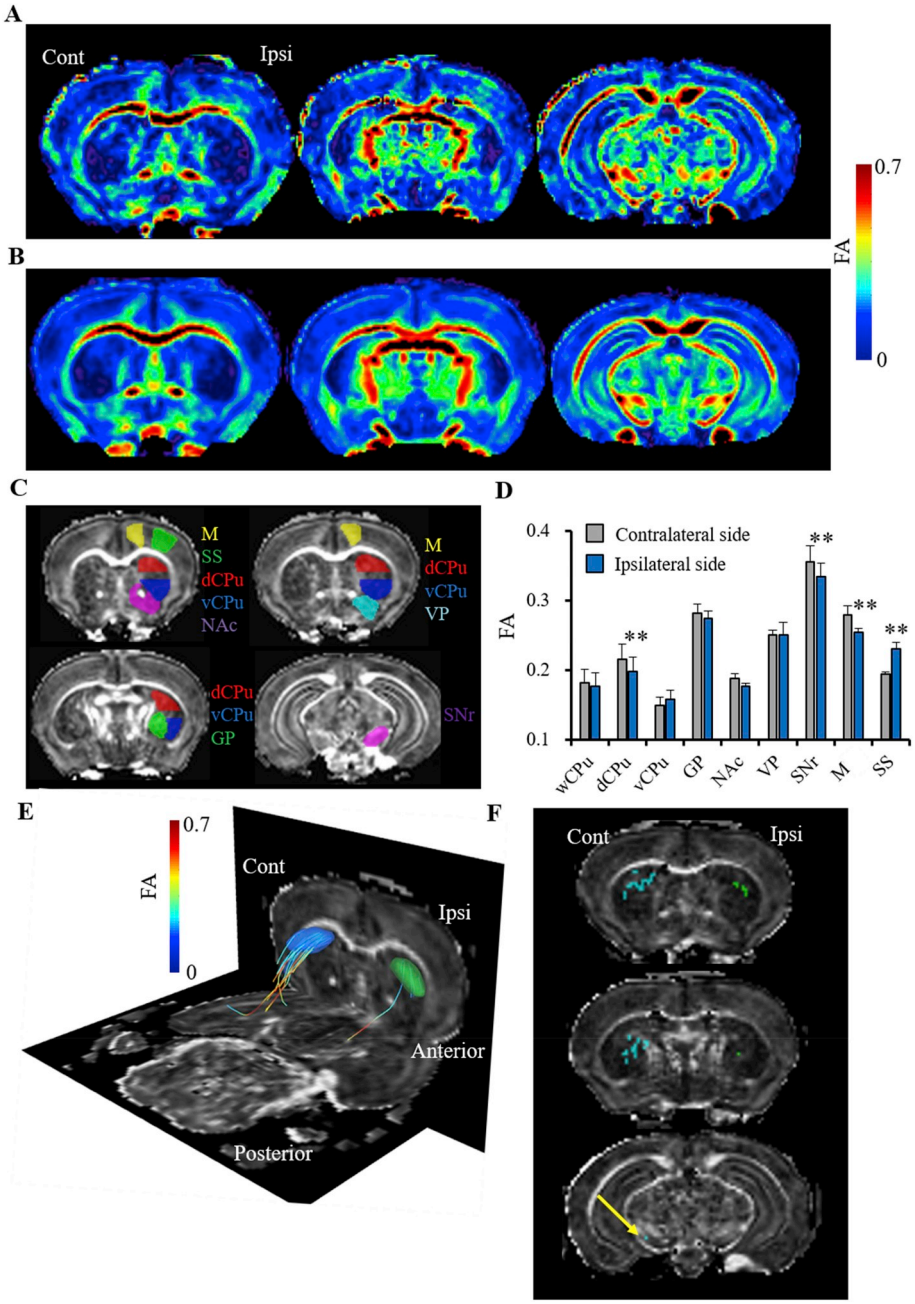

Fig. 2. DTI-FA changes induced by optogenetic stimulation. (A) Representative FA color map. (B) Averaged FA color map for 8 animals. (C) ROI images were overlaid with the grayscale FA map. (D) FA values were compared between the ipsilateral and contralateral sides (n = 8); *p < 0.05, **p < 0.01 (corrected, v.s. the contralateral side of each region). (E) The representative fiber tracts with the seeded ROIs in the ipsilateral (green) and contralateral (blue) dCPu. The color of the tract fibers indicates FA value. (F) Representative fiber tract density from Fig. 2E. The green dots indicate the tract fibers with the seeded ROI at the ipsilateral dCPu and the cyan dots show the contralateral dCPu. The yellow arrow indicates the tract fibers reaching the SNr.

(Nacalai Tesque, Inc, Japan), and 10 mg/ml salmon sperm DNA (Invitrogen, Japan). After removing the prehybridization buffer, hybridization buffer containing the following digoxigenin (DIG)-labeled cRNA probes: colony stimulating factor 1 receptor (C*sf1r*), a marker of microglia, and *Plp*, an oligodendrocyte marker, were hybridized overnight at 60 °C (Yano et al., 2018). After the sections were washed in buffers with serial differences in stringency, they were incubated with an alkaline phosphatase-conjugated anti-DIG antibody (1:5000; Roche, Japan) for 90 min at room temperature. Unbound antibody was removed by washing four times for 10 min. The cRNA probes were visualized by incubating with a freshly prepared colorimetric substrate (NBT/BCIP; Roche, Japan) overnight at room temperature. Following ISH staining, the sections were counterstained with nuclear fast red (Sigma, Japan). Images of the sections were captured using an inverted light microscope (BZ-X710, Keyence, Osaka, Japan).

2.9. Analysis of histological images

ImageJ software (http://rsb.info.nih.gov/ij/) was used for image analysis. To evaluate changes in diameter of the myelinated axons and myelin thickness using the SIM-SRM images, we targeted the ipsilateral and contralateral sides of the dCPu, vCPu, GP, SNr, M, and SS (see Figs. 3A and 5A). All images were binarized. Axon diameters of the myelinated neurons were defined as the diameter of a circle within the PLP-positive myelin. Myelin thickness was defined as the thickness of the PLP-positive area (see Fig. 3D). Axonal diameters and myelin thickness were measured from the SIM-SRM images using ImageJ. The g-ratio was calculated using equation 0.5Ad/(0.5Ad + MT), where Ad is the diameter of the axon and MT is myelin thickness (see Fig. 3C and D). Axon diameters of the MSNs were defined as the diameter of an outline of the YFP-positive circle (see Fig. 7B and C). 100 fibers per mouse were measured. The axonal diameter, myelin thickness, and g-ratio in the EM images were measured the same as for the SIM-SRM

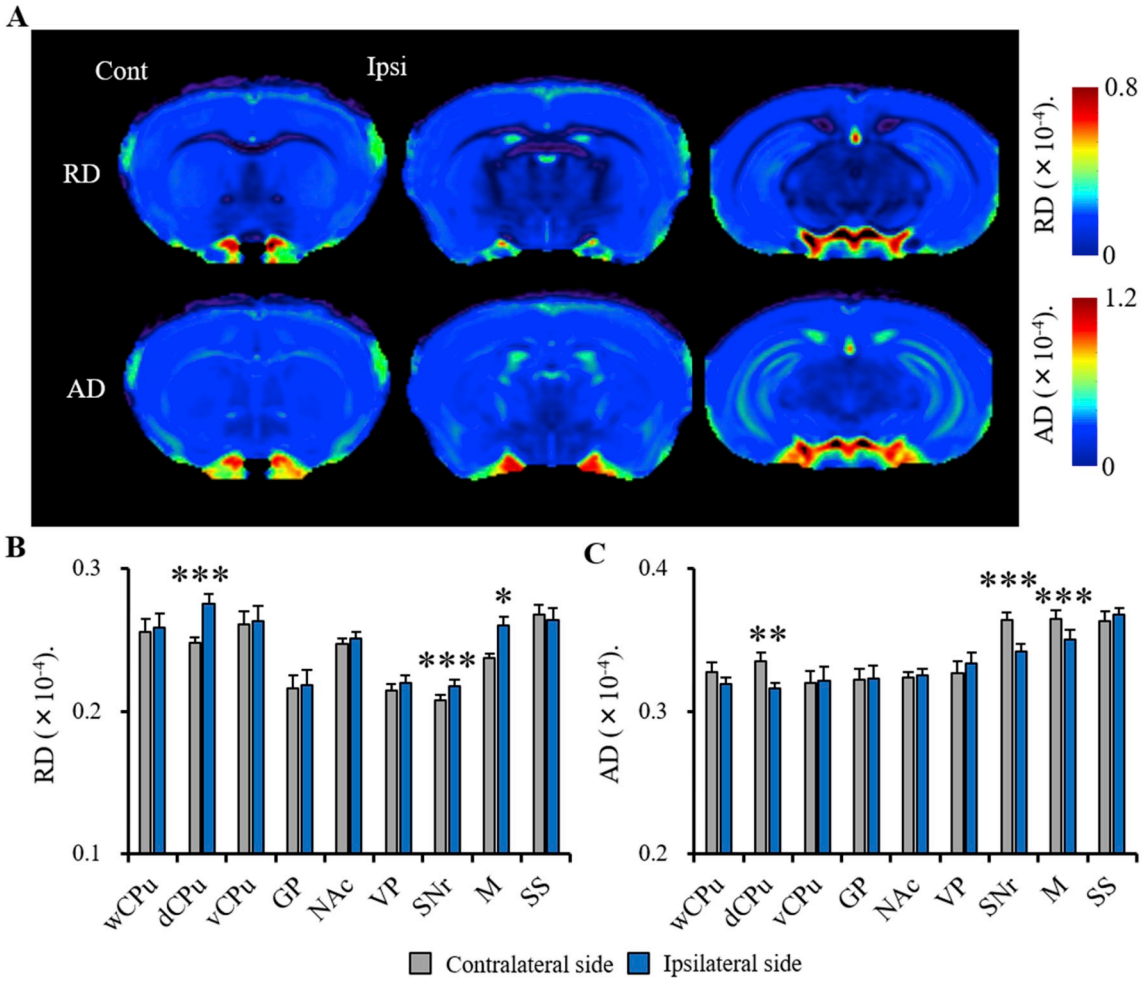

Fig. 3. Changes in RD and AD induced by optogenetic stimulation. (A) Averaged RD and AD color maps. RD (B) and AD (C) values were compared between the ipsilateral and contralateral sides (n = 8); *p < 0.05, **p < 0.01, ***p < 0.001 (corrected, v.s. the contralateral side of each region). The same ROIs as in Fig. 2C were used.

images.

Cell counts of the ISH images were performed using ImageJ to evaluate the number of microglia and oligodendrocytes. Counting regions were defined by manually co-registering them with the DTI-FA images. Cell density was calculated by dividing the number of each cell type by the area of the counting region.

2.10. Statistical processing

Statistical processing was performed using MATLAB (MathWorks, MA, USA) and Excel software (Microsoft, USA). For each data set from the DTI and histological analyses, a paired *t*-test was performed to compare the ipsilateral and contralateral sides. Bonferroni corrections were applied to correct for multiple comparisons. In order to investigate the relationship between axonal diameter and myelin thickness among the SIM-SRM and EM images, and the g-ratio and axon diameter, a Pearson's moment correlation coefficient between the two variables was calculated. All bar graphs show the mean ± standard error of the mean (SEM).

3. Results

3.1. Changes in DTI parameters in the striatal pathway

The CPu in the striatal pathway is composed of three major fiber types: 1) the cortical myelinated axons; 2) the unmyelinated axons of the striatal MSNs; and 3) the unmyelinated axons of the dopamine neurons from the substantia nigra (SN) and ventral tegmental area (VTA; Fig. 1A) (Gerfen and Surmeier, 2011; Calabresi et al., 2014). We focused on the structural impact of the MSN-mediated striatal pathway to create a simplified model of long-lasting functional change by continuously stimulating the MSNs. Double transgenic mice expressing a ChR2-YFP fusion protein in the MSNs (MSN-ChR2 mice; Fig. 1C and D) were used to induce structural information changes by long-term optogenetic stimulation to the right striatum above the skull (Fig. 1B). The ChR2-YFP protein is expressed in MSNs which have either dopamine receptor 1 (D1) or D2 (Sano et al., 2008; Bepari et al., 2012). Long-term optogenetic stimulation was continuously performed for 0.5 s per hour for 7 days, then brains were perfused and removed to conduct *ex vivo* DTI assessment (Fig. 1E). The optogenetic stimulation was activated near the dorsal caudate-putamen (dCPu), whose function is related to motor behavior (Kravitz et al., 2010). Bilateral dCPu activation promotes locomotor activity, while unilateral dCPu activation promotes rotation behaviors (Kravitz et al., 2010). To confirm the unilateral dCPu activation, we quantified the rotation behaviors during optogenetic stimulation to the right dCPu. The MSN-ChR2 mice rotated counterclockwise on the first day of stimulation induction, but the behavior was absent from the second day through the final day (Fig. 1F). This indicates that the optogenetic stimulation activated the dCPu and that long-term optogenetic stimulation of the MSNs induced motor dysfunction.

The quality of our MRI scan protocol was validated by a phantom

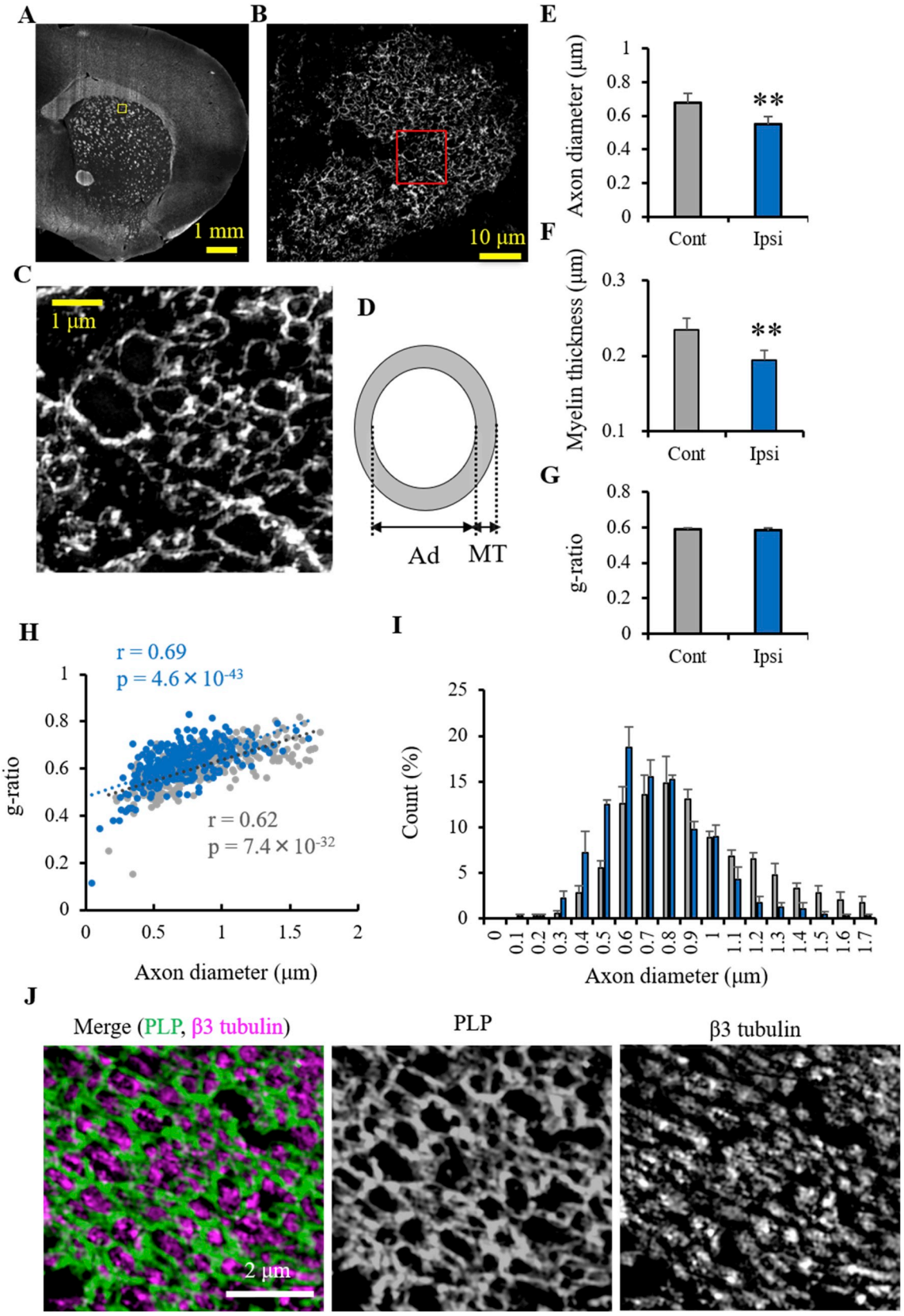

Fig. 4. Axonal changes in the myelinated fibers were detected in the dCPu by SRM. (A) A representative fluorescence microscopy image of PLP staining in the striatum. (B) A representative SRM image from the yellow boxed region in Fig. 3A. (C) A representative SRM image from the red boxed region in Fig. 3B. (D) Schematic diagram of axonal diameter (Ad) and myelin thickness (MT) measurements. The gray shading indicates the PLP-positive region. (E–G) Axon diameter (E), myelin thickness (F), and g-ratios (G) were compared in the dCPu between the ipsilateral and contralateral sides (n = 5). 100 fibers were counted per mouse and the per-animal average was used for data analysis (a total of 500 fibers were counted). (H) Correlation between axonal diameter and g-ratio of the ipsilateral and contralateral sides. (I) Histogram of axonal diameter in the dCPu between the ipsilateral and contralateral sides. (J) Representative SRM images of PLP and β3 tubulin expression; **$p < 0.01$ (paired *t*-test, vs. the contralateral side of each region).

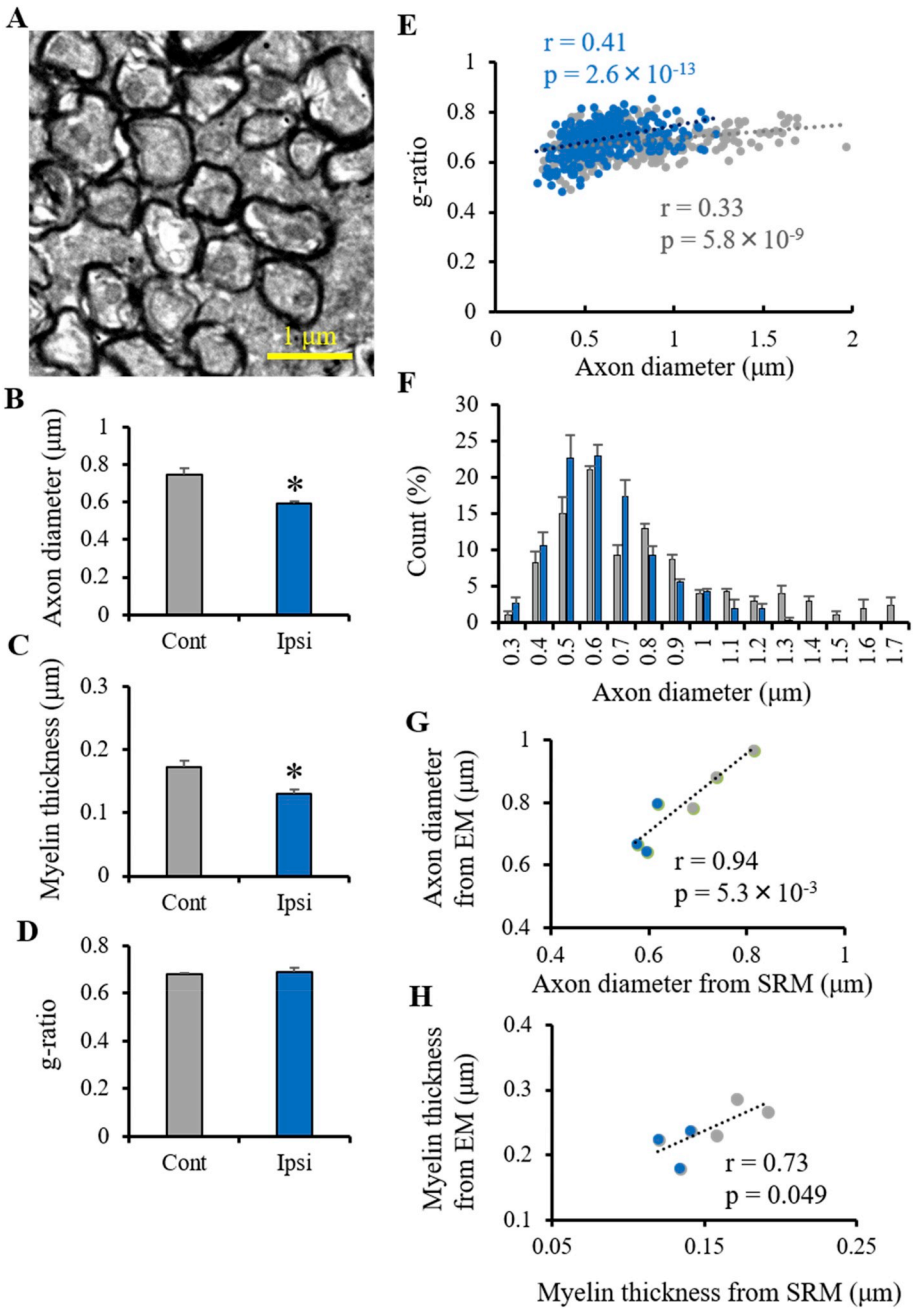

Fig. 5. Validation of axonal changes by EM. (A) Representative EM image of the myelinated axons at the dCPu. (B–D) Axonal diameter (B), myelin thickness (C), and g-ratios (D) were compared in the dCPu between the ipsilateral and contralateral sides (n = 3). 100 fibers were counted per mouse and the per-animal averages were used for data analysis (a total of 300 fibers were counted). (E) Correlation between axonal diameter and g-ratios of the ipsilateral and contralateral sides. (F) A histogram of axonal diameter in the dCPu between the ipsilateral and contralateral sides. (G–H) Correlations of axonal diameter (G) and myelin thickness (H) between SRM and EM; *p < 0.05 (paired *t*-test, vs. the contralateral side of each region).

experiment. We obtained T1-weighted images, and raw images of the phantom were obtained by DTI at b = 0 and 1500 s/mm^2 to confirm the magnetic homogeneity (Supplementary Fig. 1B). Raw images from DTI of mouse brains were also obtained (Supplementary Fig. 1A). We also checked for motion artifacts during our long acquisition of DTI images (Supplementary Fig. 1C). Motion of the phantom images by DTI were within one tenth or less of 1 voxel size (0.125 mm).

Ex vivo DTI was performed on brains that had been continuously stimulated at the right-side striatum. The individual FA maps and the averaged FA map for all animals were calculated to compare the FA value between the ipsilateral and contralateral sides (Fig. 2A and B). The ROIs were identified in the striatal pathway (wCPu, dCPu, vCPu, NAc, GP, VP, and SNr) and the cortex (M and SS) of each side (Fig. 2C). The FA values in the dCPu (0.183 ± 0.012 on the ipsilateral side, 0.201 ± 0.013 on the contralateral side; p = 0.001), SNr (0.334 ± 0.011, 0.361 ± 0.012; p = 0.002), and M (0.256 ± 0.005, 0.282 ± 0.007; p = 0.004) of the ipsilateral side were significantly lower than on the contralateral side. FA at the SS (0.231 ± 0.007, 0.200 ± 0.007; p = 0.003) of the ipsilateral side was higher than that of the contralateral side (Fig. 2D). FA did not change at the wCPu (0.163 ± 0.012, 0.169 ± 0.011; p = 0.053), vCPu (0.140 ± 0.010, 0.142 ± 0.007; p = 0.76), GP (0.268 ± 0.013, 0.272 ± 0.011; p = 0.76), NAc (0.178 ± 0.003, 0.183 ± 0.005; p = 0.53), nor VP (0.271 ± 0.011, 0.269 ± 0.008; p = 0.76). The averaged RD and AD maps for all animals were calculated to compare the RD and AD values between the ipsilateral and contralateral sides (Fig. 3A). The RD values in the dCPu (0.276 ± 0.006 × 10^{-4} on the ipsilateral side, 0.248 ± 0.004 × 10^{-4} on the contralateral side; p = 0.0007), SNr (0.218 ± 0.004 × 10^{-4}, 0.208 ± 0.003 × 10^{-4}; p = 0.0001), and M (0.260 ± 0.006 × 10^{-4}, 0.238 ± 0.002 × 10^{-4}; p = 0.027) of the ipsilateral side were significantly higher than on the contralateral side (Fig. 3B). The AD values in the dCPu (0.316 ± 0.004 × 10^{-4} on the ipsilateral side, 0.335 ± 0.006 × 10^{-4} on the contralateral side; p = 0.001), SNr (0.342 ± 0.005 × 10^{-4}, 0.364 ± 0.005 × 10^{-4};

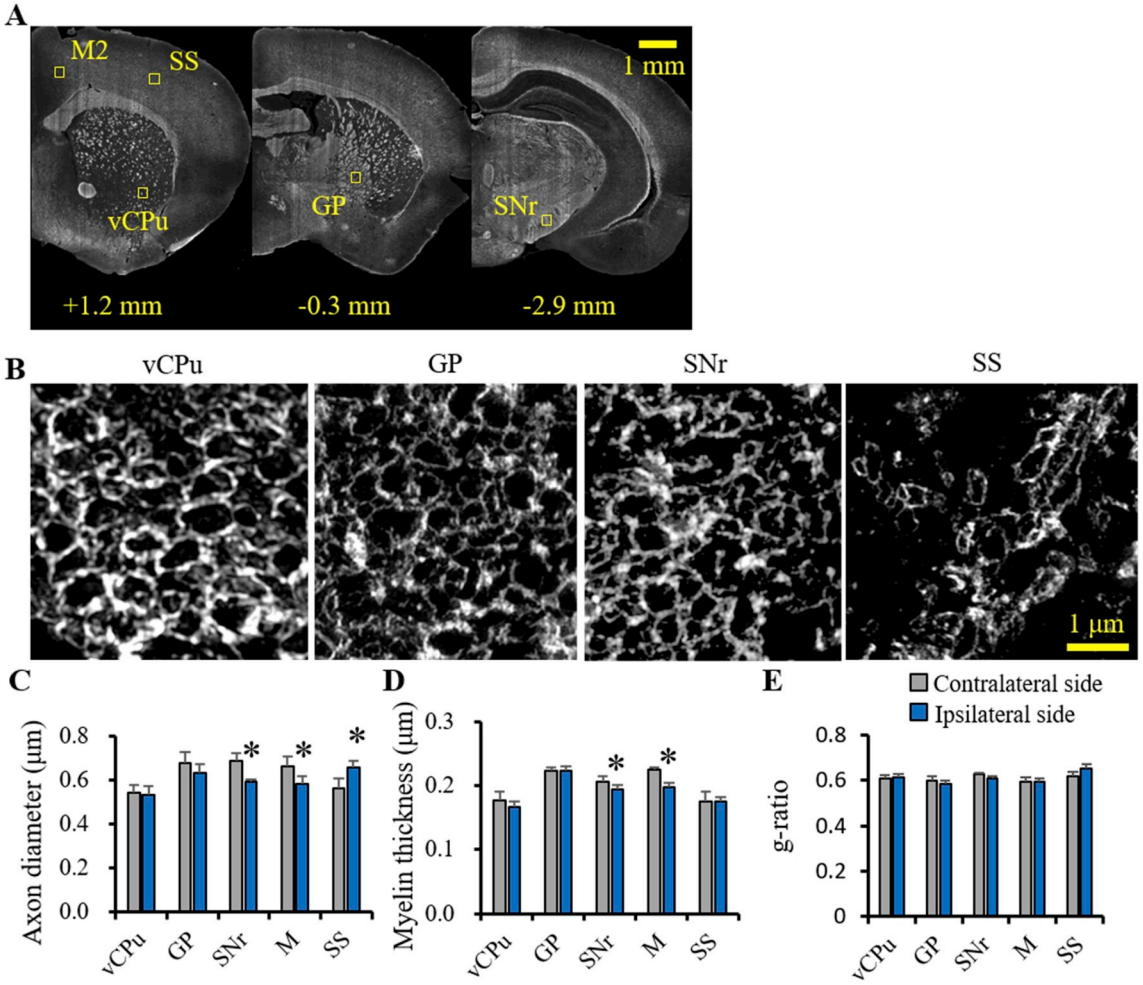

Fig. 6. Axonal changes to the myelinated fibers in the striatal pathway and cortex. (A) Images of PLP staining. The numbers at the bottom are the distances from the bregma. (B) Representative SRM images of PLP expression in the vCPu, GP, SNr, and M in the yellow boxed regions from Fig. 5A. (C–E) Axonal diameter (C), myelin thickness (D), and g-ratios (E) were compared at the vCPu, GP, SNr, M, and SS between the ipsilateral and contralateral sides (n = 5). 100 fibers from each region were counted per mouse and the per-animal average was used for data analysis (a total of 400 fibers from each region were counted); *p < 0.05 (corrected, v.s. the contralateral side of each region).

p = 0.0004), and M ($0.351 \pm 0.007 \times 10^{-4}$, $0.265 \pm 0.006 \times 10^{-4}$; p = 0.0002) of the ipsilateral side were significantly lower than on the contralateral side (Fig. 3C).

DTI-tractography was performed to investigate the tract fibers associated with the seeded ROI at the dCPu. These tract fibers included the MSN axons, the cortical axons running across the striatum, and the axons of the dopaminergic neurons from the substantia nigra (SN) and ventral tegmental area (VTA). The number of tract fibers from the dCPu of the ipsilateral side was less than that of the contralateral side (Fig. 2E). Tract density maps showed a decrease in the density of the tract fibers from the dCPu at the GP and SNr. These results indicated a reduction of FA in the dorsal striatal pathway.

3.2. Structural changes in the myelinated axons of the striatal pathway detected by SIM-SRM

We can infer that the reduction in FA primarily resulted from decreased myelin content and/or axonal damage (Zerbi et al., 2013; Falangola et al., 2014; Kelm et al., 2016; Chang et al., 2017; Yano et al., 2018), suggesting that change in FA is tightly associated with structural changes in the myelinated neurons. We first focused on the structural changes to the bundles of the myelinated axons at the dCPu (Fig. 4A). These myelinated axons derive from the axons of the cortical neurons and penetrate the striatum. To investigate the precise structural changes, we utilized SIM-SRM imaging of the PLP-IHC which labeled myelin. The PLP images obtained by SIM-SRM showed the specific myelin content (Fig. 4B and C). The PLP-positive circles in Fig. 3C are cross sections of the myelin sheets, and the areas within the circles are cross sections of the myelinated axons. These regions were confirmed by double IHC for PLP and beta-3 tubulin, a marker of neural fibers (Fig. 4J). These results demonstrated that PLP IHC combined with SIM-SRM can be used to measure the diameter of myelinated axons (Ad) their myelin thickness (MT), and g-ratio, the ratio between diameter and myelin thickness (Fig. 4D). The diameter (0.54 ± 0.04 μm on the ipsilateral side, 0.67 ± 0.05 μm on the contralateral side; p = 0.009) and myelin thickness (0.19 ± 0.01 μm, 0.23 ± 0.01 μm; p = 0.006) of the myelinated axons in the ipsilateral dCPu were significantly lower than in the contralateral dCPu (Fig. 4E and F), although the g-ratio (0.58 ± 0.01, 0.58 ± 0.01; p = 0.51) did not change (Fig. 4G). The axon diameters from both sides of the dCPu showed significant correlation with the g-ratio (Fig. 4H). Histograms of axonal diameter at the dCPu also showed this reduction in diameter (Fig. 4I).

To confirm the changes in axonal diameter and myelin thickness at the dCPu, we also compared them using EM images (Fig. 5A). Serial brain sections were used to compare the differences between SIM-SRM and EM observations. The diameter (0.59 ± 0.01 μm on the ipsilateral side, 0.74 ± 0.04 μm on the contralateral side; p = 0.025) and myelin thickness (0.13 ± 0.006 μm, 0.17 ± 0.009 μm; p = 0.043) of the

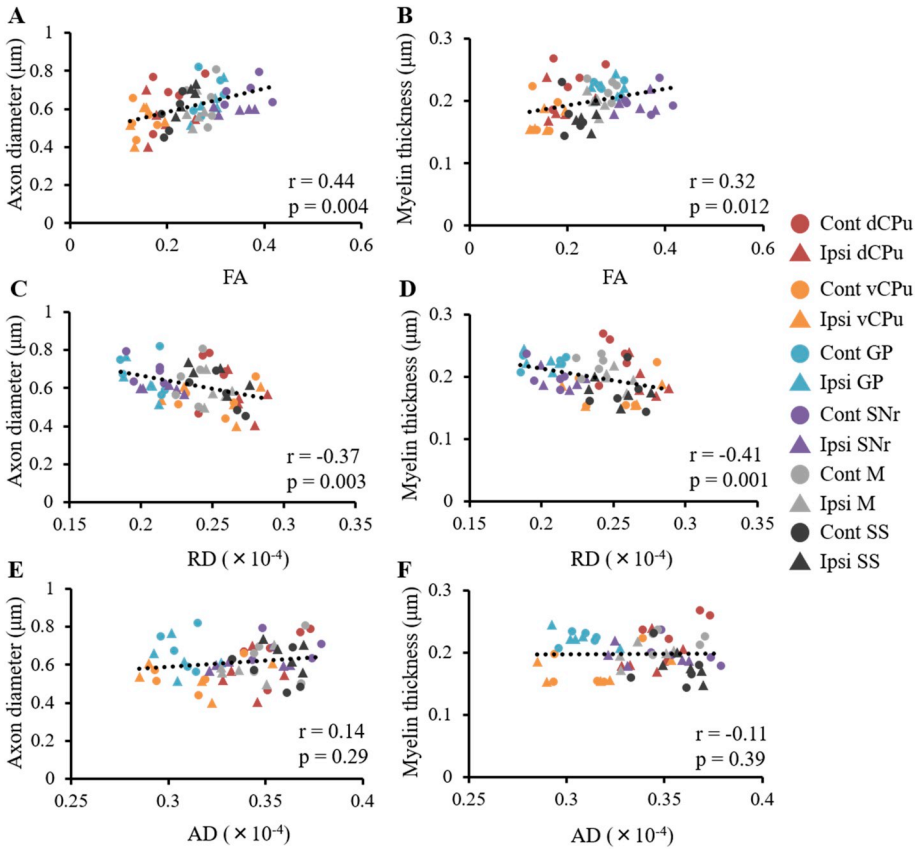

Fig. 7. Correlation between DTI and histological data. Graphs showing the correlation between DTI results (A, B: FA; C, D: RD; and E, F: AD) and histological data of the myelinated axons (axonal diameter shown at left in A, C, E; myelin thickness shown at right in B, D, F) in the dCPu, vCPu, GP, SNr, M, and SS of the ipsilateral and contralateral sides. The circles indicate the contralateral side, triangles indicate the ipsilateral side. The dashed lines indicate correlations between DTI parameters and histological data.

myelinated axons in the ipsilateral dCPu were significantly lower than those of the contralateral dCPu (Fig. 5B and C), although the g-ratio (0.69 ± 0.01, 0.68 ± 0.01; p = 0.51) did not change (Fig. 5D). The axon diameters on both sides of the dCPu showed significant correlation with the g-ratio, respectively (Fig. 5E); however, the correlation coefficient from EM was smaller than that of SIM-SRM. The histograms of the axonal diameters at the dCPu also showed decreased diameters (Fig. 5F). Axonal diameter and myelin thickness detected by SIM-SRM and EM were highly correlated (Fig. 5G and H), indicating that the structural changes detected by SIM-SRM are accurate.

Next, we investigated structural changes in other regions (vCPu, GP, SNr, M, and SS) using the same SIM-SRM methods with PLP-IHC (Fig. 6A and B). Axonal diameters on the ipsilateral side were significantly lower in the SNr and M than those on the contralateral side, and were significantly higher in the SS (Fig. 6C). Myelin thickness on the ipsilateral side was significantly lower in the SNr and M (Fig. 6D), and the g-ratio was not significantly changed compared to the contralateral side (Fig. 6E). When we compared the correlation between the DTI data (FA, RD, and AD) and histological data (axon diameter and myelin thickness), axon diameter showed a significant positive correlation with FA and significant negative correlation with RD (Fig. 7A, C). Myelin thickness also showed a significant positive correlation with FA and negative correlation with RD (Fig. 7B, D). AD did not show significant correlations with axon diameter or myelin thickness (Fig. 7E and F).

ISH using RNA probes specific to microglia and oligodendrocytes was performed to evaluate the effect of inflammation resulting from long-term optogenetic stimulation and to evaluate how the number of oligodendrocytes affects FA change, respectively (Fig. 8A and B). The number of microglia did not change between the ipsilateral and contralateral sides of the striatum (dCPu and vCPu; Fig. 8C), indicating that long-term optogenetic stimulation does not induce inflammation. The number of oligodendrocytes also did not change between the ipsilateral and contralateral sides of the dCPu, vCPu, GP, SNr, M, and SS (Fig. 8B), indicating that the number of oligodendrocytes did not affect the changes in FA.

3.3. Structural changes in MSN fibers detected by SIM-SRM

The structural changes to the MSNs were investigated using SIM-SRM analysis of GFP-IHC (used to enhance the ChR2-YFP signal). YFP was found to be expressed in the striatal pathway (dCPu, vCPu, GP, SNr; Fig. 9A), and the SIM-SRM images identified the specific MSN fibers (Fig. 7C). Most fibers in the CPu were dendritic MSN fibers. All fibers in the GP and SNr were axonal MSN fibers (unmyelinated axons), specifically axonal fibers of the D1-MSNs (Kravitz et al., 2010; Nishi et al., 2011). The outlines of the YFP-positive fibers shown in Fig. 9C are cross-sections of the MSN dendrites in the dCPu and vCPu, and MSN axons in the GP and SNr. Given that ChR2 is a membranous protein, the width of the surrounding YFP-positive region represents the diameter of the MSN fibers (Fig. 9B). Analysis showed that the MSN dendrites on the ipsilateral side were significantly smaller in the dCPu than those on the contralateral side, but were unchanged in the vCPu (Fig. 9D). The MSN axons were also significantly smaller in the GP and SNr (Fig. 9D).

4. Discussion

In the present study, we found that long-term optogenetic stimulation of the MSNs induces changes in DTI parameters (FA, RD, and AD) in the striatal pathway (dCPu and SNr) and the motor and somatosensory cortex on the ipsilateral side relative to the contralateral side (Figs. 2 and 3). Observations using SIM-SRM of PLP-IHC found reductions in axonal diameter and myelin thickness of the myelinated cortical fibers in the same regions identified by DTI (Figs. 4–6). These structural changes detected histologically were correlated with the structural changes detected by DTI (Fig. 7). Additionally, we also found

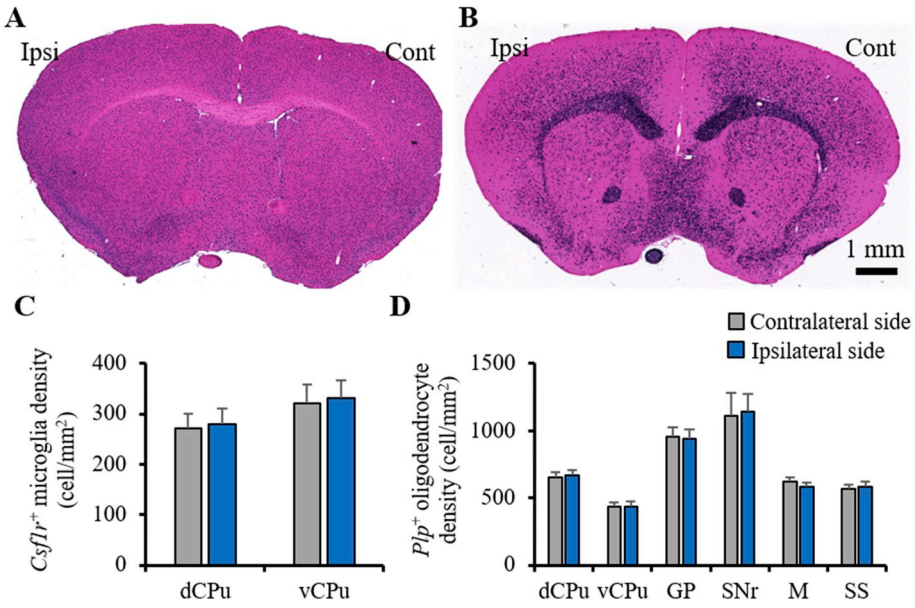

Fig. 8. The numbers of microglia and oligodendrocytes were not affected. (A–B) Representative ISH images of cfms (A) and PLP (B) expression. (C) The number of C*sf1r*-positive cells (microglia) was compared in the dCPu and vCPu between the ipsilateral and contralateral sides (n = 5). (D) The number of *Plp*-positive cells (oligodendrocytes) was compared in the dCPu, vCPu, GP, SNr, M, and SS between the ipsilateral and contralateral sides (n = 5).

reductions in the dendritic and axonal diameters of the MSNs following the stimulation (Fig. 9). These results indicate that long-term neural activation of the MSNs induces structural changes in the striatal pathway.

In general, fMRI studies provide comprehensive functional network imaging. However, the blood oxygenation level-dependent (BOLD) signal in fMRI may fail to reflect actual neural activity (Veldsman et al., 2015; Abe et al., 2017). At the striatum, in particular, the BOLD signal exhibits an opposite signal from the neural activity (Shih et al., 2009, 2014), suggesting that the BOLD signal in the striatum, which was targeted in the current study, likely did not act as a neuronal marker. In contrast, DTI assessment is applicable to the detection of structural information changes throughout the entire brain. It has been shown that a decrease in FA mirrors abnormalities in the pathological state of both myelin content and neural fibers (Zerbi et al., 2013; Falangola et al., 2014; Kelm et al., 2016; Chang et al., 2017; Yano et al., 2018). However, using only the changes in DTI parameters we were not able to determine the precise structural changes and thus required further histological analysis. Results from DTI could only indicate the region in which the pattern of myelin content and/or neural fibers was changed. Therefore, additional histological analysis is required to identify the precise structural changes. SIM-SRM imaging is a more powerful technique than confocal microscopy for easily obtaining high-resolution images for visualization of micro-structural changes. The current study demonstrated a successful new strategy for identifying structural changes induced by long-term optogenetic stimulation. This involves comprehensive imaging by DTI to survey the regions where structural change has occurred, followed by precise histological imaging using SIM-SRM and EM to identify the actual structural change.

The FA value is a summary measure of microstructural integrity and

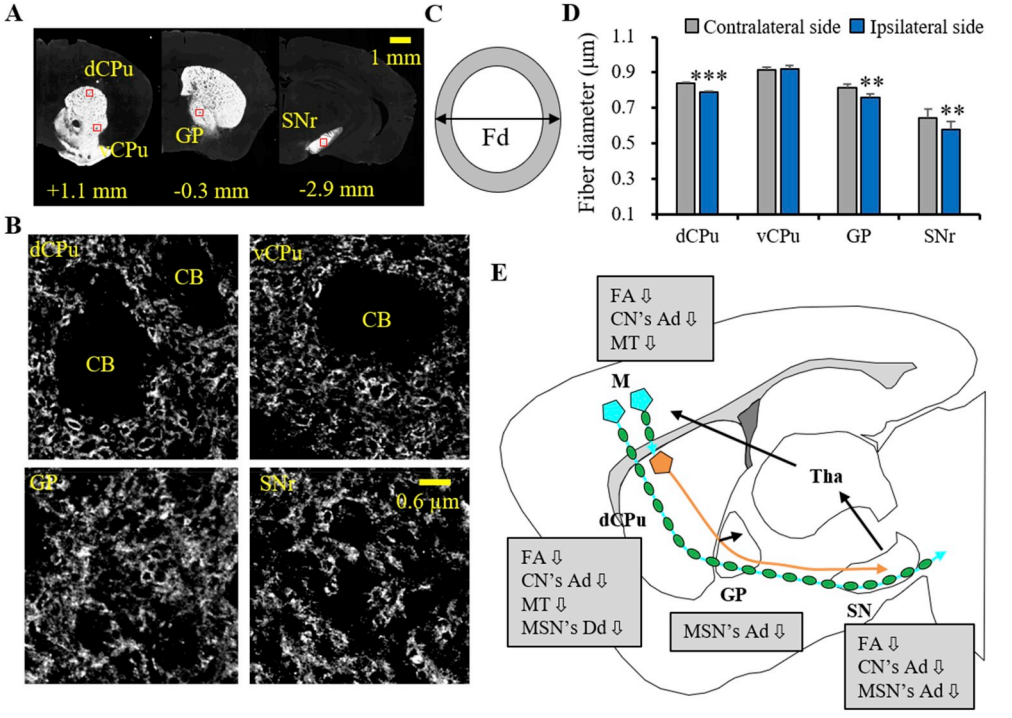

Fig. 9. Changes in MSN fiber diameter. (A) Representative YFP images obtained by fluorescence microscopy. The numbers at the bottom are the distances from the bregma. (B) Representative SRM images of YFP expression in the dCPu, vCPu, GP, and SNr; CB: cell body. (C) Schematic diagram of fiber diameter measurements (Fd); gray shading represents the YFP-positive region. (D) Fiber diameter was compared in the dCPu, vCPu, GP, and SNr between the ipsilateral and contralateral sides (n = 4). 100 fibers were counted per mouse and the per-animal averages were used for data analysis (a total of 400 fibers were counted); $^{**}p < 0.01$, $^{***}p < 0.001$ (corrected, v.s. the contralateral side of each region). (E) Schematic diagram summarizing the structural changes in FA and the histological data (cortical neuron [CN] axon diameter [Ad], MSN dendrite diameter [Dd], MSN AD, and myelin thickness [MT]).

the observed reduction in FA likely reflects microstructural changes in fibers and myelin content. Animal experiments showing myelin dysfunction (demyelination by cuprizone treatment, traumatic brain injury, or neurodegenerative disease) have identified decreases in FA accompanied by structural disruptions in axons and myelin (Müller et al., 2013; Zerbi et al., 2013; Hemanth Kumar et al., 2014; Laitinen et al., 2015; Yano et al., 2018; Montagne et al., 2018). Conversely, mice which underwent motor skill learning, leading to increased myelination, exhibited an increase in FA (Sampaio-Baptista et al., 2013). Many animal DTI studies have suggested that an increase in RD is an indicator of demyelination and/or axonal damage and that a decrease in AD is indicative of damage to axonal fibers (Zerbi et al., 2013; Falangola et al., 2014; Guglielmetti et al., 2016; Kelm et al., 2016; Chang et al., 2017; Yano et al., 2018). However, there is ongoing debate as to whether DTI signals arise more from the intra or extra axonal space, and this dispute remains wholly unresolved. Many other factors (e.g. fiber density, cell density, and synapse density) could also contribute to the changes in DTI parameters, especially as measured here with a single b-value ($b = 1500\ s/mm^2$). In the current study, we did not evaluate all possible factors that could contribute to changes in DTI parameters, but focused on oligodendrocyte and microglial densities which were found not to contribute to changes in DTI parameters (Fig. 8).

Our DTI data show increases in RD, and reductions in AD and FA at the dCPu, SNr, and M after long-term optogenetic stimulation (Figs. 2 and 3). From these DTI data, we can infer the structural effects on the fibers and/or myelin content at the dCPu, SNr, and M. We then focused on the regions identified by DTI to perform high-resolution histological assessment with SIM-SRM. This histological approach confirmed the decrease in axonal diameter and myelin thickness of the myelinated cortical neurons and reductions in the dendritic and axonal diameter of the MSNs. In addition, these histological data were highly correlated with the DTI data. This correlation between DTI and the histological data was also supported by our previous report (Yano et al., 2018) and reports by other groups (Falangola et al., 2014; Kelm et al., 2016; Chang et al., 2017), further indicating that FA and RD reflect the structural status of axons and myelin. These results suggest that long-term optogenetic stimulation of the MSNs results in decreased axonal diameters of both the cortical neurons and MSNs. These structural changes detected by both DTI and histological analyses also confirmed that the changes in DTI parameters reflect a reduction in the diameter of myelinated axons of the cortical neurons. Additionally, we found a reduction in the diameter of unmyelinated axons and dendrites of the MSNs following long-term optogenetic stimulation. These data clearly indicate that DTI with specific optogenetic stimulation of the MSNs can detect structural alterations in the cortical neurons (likely motor cortex neurons) as well as the MSNs.

One major question posed by the present results is why long-term stimulation of the MSNs causes a decrease in axonal and dendritic diameter. This finding was supported by a previous study of deep brain stimulation (DBS) using optogenetics that showed that low-frequency optogenetic stimulation of the NAc induced long-term depression (LTD) (Creed et al., 2015). This LTD likely led to neural dysfunction evidenced by a decrease in spine density and morphology (Zhou et al., 2004; Wiegert and Oertner, 2013); however, these papers did not investigate diameter changes in MSN axons. These changes caused by long-term optogenetic stimulation likely reduced nerve conduction velocity (Waxman, 1980; Gillespie and Stein, 1983). Another question raised by this study pertains to why the myelinated cortical axons (ChR2-negative) are affected by stimulation of the MSNs (ChR2-positive). Based on the changes in DTI parameters at the M, it is possible that the affected cortical axons are from the motor cortex. One possible explanation for this effect is that the long-term activation of the dorsal striatal pathway (the D1-MSN mediated direct pathway), which is related to motor function, alters the neurons in the motor cortex via the cortico-striatal-thalamo-cortical circuit (Fig. 9E). Indeed, our continuous optogenetic stimulation induced an impairment in motor behavior (Fig. 1F). Interestingly, we found an increase in FA and axonal diameter in the somatosensory cortex after long-term stimulation. While we are not able to address why the long-term stimulation increased FA at this stage, the results suggest that the affected cortical axons in the striatum may not be from the somatosensory cortex. However, further analysis will be required to identify the effect of long-term stimulation on the motor cortex.

There is a limitation in the optogenetic stimulation used in the current study. We performed unilateral optogenetic LED stimulation in the mouse skull. We assumed that this stimulation activated only the ipsilateral striatum due to the rotation behaviors observed in mice (Fig. 1F). If the striatum were activated bilaterally, the mice should exhibit locomotor activity (Kravitz et al., 2010). However, we cannot completely rule out that our long-term optogenetic stimulation did not affect the contralateral striatum. Indeed, the mice did not exhibit rotation behaviors after the second day of stimulation (Fig. 1F). This implies that chronic neural activation of the MSNs likely also affects the contralateral MSNs. In our study, we investigated the changes in DTI parameters and histological structures after long-term stimulation. Therefore, we only evaluated structural changes between the ipsilateral and contralateral sides in which chronic effects resulting from long-term activation in MSNs were evident. To confirm the presence of these chronic effects, additional studies are needed in which we compare structural changes with morphology in sham control mice.

In general, histological analysis of axons, myelin, and their g-ratio has been performed by electron microscopy. In the current study, PLP-IHC with SIM-SRM analysis revealed a decrease in axonal diameter and myelin thickness. Our histological approach using SIM-SRM provided clear and detailed myelin imaging enabling us to analyze myelin thickness, axon diameter, and their g-ratio (Fig. 4). These axon and myelin analyses were also confirmed by EM (Fig. 5). When the images obtained by SIM-SRM and EM were compared, axonal diameter and myelin thickness by SIM-SRM were lower than for EM, although the g-ratios were almost the same. This is possibly due to shrinkage of the axons and myelin during preparation of the EM samples. Moreover, when the sample processing times are compared, IHC with SIM-SRM (2 days) is easier and faster than EM (at least 1 week). Our histochemical approach suggested that PLP-IHC combined with SIM-SRM analysis is more useful for the evaluation of myelin content and myelinated axons than EM analysis. Furthermore, analysis of GFP-IHC by SIM-SRM enabled the specific imaging of unmyelinated axons expressing ChR2-YFP. Together, the combined approach of IHC with SIM-SRM provided precise and detailed imaging of the myelinated and unmyelinated axons and myelin content as well as the added benefit of shorter sample preparation times compared to EM.

5. Conclusion

We found that long-term activation of MSNs, which results in motor dysfunction, induced reductions in the diameter of MSN axons and dendrites as well as reductions in the myelinated cortical axons when comparing the ipsilateral and contralateral sides. Thus, the use of DTI and post-hoc histological assessment with super-resolution microscopy identified that long-term optogenetic stimulation of MSNs induces structural alterations to the striatal pathway. This combination technique provides a tool for understanding the causal relationship between functional and structural alterations.

Acknowledgements

We thank Nobuko Moritoki for support in preparing the samples for electron microscopy and in obtaining the electron microscopy images. We thank the Collaborative Research Resources, Keio University School of Medicine for technical assistance with the Zeiss ELYRA 3D-SIM system. This work was supported by a Grant-in-Aid for Research

Fellowships of the Japan Society for the Promotion of Science (JSPS Research Fellow) under grant number 18J00922(Y.A.); Takeda Science Foundation (Y.A.); Grant-in-Aid for Scientific Research (B) under grant number 15H03123(K.F.T.); and a grant from Brain Mapping by Integrated Neurotechnologies for Disease Studies (Brain/MINDS) by AMED under grant number JP18dm0207002(Y.A., Y.K., F.S., S.S. and K.F.T.) and JP18dm0207001 (H.O.).

Appendix A. Supplementary data

Supplementary data to this article can be found online at https://doi.org/10.1016/j.neuint.2019.02.017.

References

Abe, Y., Tsurugizawa, T., Le Bihan, D., 2017. Water diffusion closely reveals neural activity status in rat brain loci affected by anesthesia. PLoS Biol. 15 (4), e2001494.
Alexander, A.L., Lee, J.E., Lazar, M., Field, A.S., 2007. Diffusion tensor imaging of the brain. Neurotherapeutics 4 (3), 316–329.
Basser, P.J., Mattiello, J., Le Bihan, D., 1994a. MR diffusion tensor spectroscopy and imaging. Biophys. J. 66 (1), 259–267.
Basser, P.J., Mattiello, J., Le Bihan, D., 1994b. Estimation of the effective self-diffusion tensor from the NMR spin echo. J. Magn. Reson. B 103 (3), 247–254.
Bepari, A.K., Sano, H., Tamamaki, N., Nambu, A., Tanaka, K.F., Takebayashi, H., 2012. Identification of optogenetically activated striatal medium spiny neurons by Npas4 expression. PLoS One 7 (12), e52783.
Bronfeld, M., Bar-Gad, I., 2011. Loss of specificity in Basal Ganglia related movement disorders. Front. Syst. Neurosci. 3, 5–38.
Calabresi, P., Picconi, B., Tozzi, A., Ghiglieri, V., Di Filippo, M., 2014. Direct and indirect pathways of basal ganglia: a critical reappraisal. Nat. Neurosci. 17 (8), 1022–1030.
Chang, E.H., Argyelan, M., Aggarwal, M., Chandon, T.S., Karlsgodt, K.H., Mori, S., Malhotra, A.K., 2017. The role of myelination in measures of white matter integrity: combination of diffusion tensor imaging and two-photon microscopy of CLARITY intact brains. Neuroimage 147, 253–261.
Creed, M., Pascoli, V.J., Lüscher, C., 2015. Addiction therapy. Refining deep brain stimulation to emulate optogenetic treatment of synaptic pathology. Science 347 (6222), 659–664.
Dazai, J., Spring, S., Cahill, L.S., Henkelman, R.M., 2011. Multiple-mouse neuroanatomical magnetic resonance imaging. JoVE 48, e2497.
Falangola, M.F., Guilfoyle, D.N., Tabesh, A., Hui, E.S., Nie, X., Jensen, J.H., Gerum, S.V., Hu, C., LaFrancois, J., Collins, H.R., Helpern, J.A., 2014. Histological correlation of diffusional kurtosis and white matter modeling metrics in cuprizone-induced corpus callosum demyelination. NMR Biomed. 27 (8), 948–957.
Feldman, H.M., Yeatman, J.D., Lee, E.S., Barde, L.H., Gaman-Bean, S., 2010. Diffusion tensor imaging: a review for pediatric researchers and clinicians. J. Dev. Behav. Pediatr. 31 (4), 346–356.
Gerfen, C.R., Surmeier, D.J., 2011. Modulation of striatal projection systems by dopamine. Annu. Rev. Neurosci. 34, 441–466.
Gillespie, M.J., Stein, R.B., 1983. The relationship between axon diameter, myelin thickness and conduction velocity during atrophy of mammalian peripheral nerves. Brain Res. 259 (1), 41–56.
Guglielmetti, C., Veraart, J., Roelant, E., Mai, Z., Daans, J., Van Audekerke, J., Naeyaert, M., Vanhoutte, G., Delgado, Y., Palacios, R., Praet, J., Fieremans, E., Ponsaerts, P., Sijbers, J., Van der Linden, A., Verhoye, M., 2016. Diffusion kurtosis imaging probes cortical alterations and white matter pathology following cuprizone induced demyelination and spontaneous remyelination. Neuroimage 125, 363–377.
Hemanth Kumar, B.S., Mishra, S.K., Trivedi, R., Singh, S., Rana, P., Khushu, S., 2014. Demyelinating evidences in CMS rat model of depression: a DTI study at 7 T. Neuroscience 275, 12–21.
Hikosaka, O., Takikawa, Y., Kawagoe, R., 2000. Role of the basal ganglia in the control of purposive saccadic eye movements. Physiol. Rev. 80 (3), 953–978.
Inamura, N., Sugio, S., Macklin, W.B., Tomita, K., Tanaka, K.F., Ikenaka, K., 2012. Gene induction in mature oligodendrocytes with a PLP-tTA mouse line. Genesis 50 (5), 424–428.
Kelm, N.D., West, K.L., Carson, R.P., Gochberg, D.F., Ess, K.C., Does, M.D., 2016. Evaluation of diffusion kurtosis imaging in ex vivo hypomyelinated mouse brains. Neuroimage 124 (Pt A), 612–626.
Kravitz, A.V., Freeze, B.S., Parker, P.R., Kay, K., Thwin, M.T., Deisseroth, K., Kreitzer, A.C., 2010. Regulation of parkinsonian motor behaviours by optogenetic control of basal ganglia circuitry. Nature 466 (7306), 622–626.
Laitinen, T., Sierra, A., Bolkvadze, T., Pitkänen, A., Gröhn, O., 2015. Diffusion tensor imaging detects chronic microstructural changes in white and gray matter after traumatic brain injury in rat. Front. Neurosci. 9, 128.
Le Bihan, D., Mangin, J.F., Poupon, C., Clark, C.A., Pappata, S., Molko, N., Chabriat, H., 2001. Diffusion tensor imaging: concepts and applications. J. Magn. Reson. Imag. 13 (4), 534–546.
Mito, M., Kawaguchi, T., Hirose, T., Nakagawa, S., 2016. Simultaneous multicolor detection of RNA and proteins using super-resolution microscopy. Methods 98, 158–165.
Montagne, A., Nikolakopoulou, A.M., Zhao, Z., Sagare, A.P., Si, G., Lazic, D., Barnes, S.R., Daianu, M., Ramanathan, A., Go, A., Lawson, E.J., Wang, Y., Mack, W.J., Thompson, P.M., Schneider, J.A., Varkey, J., Langen, R., Mullins, E., Jacobs, R.E., Zlokovic, B.V., 2018. Pericyte degeneration causes white matter dysfunction in the mouse central nervous system. Nat. Med. 24 (3), 326–337.
Mori, S., Zhang, J., 2006. Principles of diffusion tensor imaging and its applications to basic neuroscience research. Neuron 51 (5), 527–539.
Müller, H.P., Kassubek, J., Vernikouskaya, I., Ludolph, A.C., Stiller, D., Rasche, V., 2013. Diffusion tensor magnetic resonance imaging of the brain in APP transgenic mice: a cohort study. PLoS One 8 (6), e67630.
Nambu, A., 2005. A new approach to understand the pathophysiology of Parkinson's disease. J. Neurol. 252 (Suppl. 4), 1–4.
Nambu, A., Chiken, S., Shashidharan, P., Nishibayashi, H., Ogura, M., Kakishita, K., Tanaka, S., Tachibana, Y., Kita, H., Itakura, T., 2011. Reduced pallidal output causes dystonia. Front. Syst. Neurosci. 28 (5), 89.
Nishi, A., Kuroiwa, M., Shuto, T., 2011. Mechanisms for the modulation of dopamine d(1) receptor signaling in striatal neurons. Front. Neuroanat. 5, 43.
Sagi, Y., Tavor, I., Hofstetter, S., Tzur-Moryosef, S., Blumenfeld-Katzir, T., Assaf, Y., 2012. Learning in the fast lane: new insights into neuroplasticity. Neuron 73 (6), 1195–1203 J. Neurosci. 33(50), 19499-19503.
Sampaio-Baptista, C., Khrapitchev, A.A., Foxley, S., Schlagheck, T., Scholz, J., Jbabdi, S., DeLuca, G.C., Miller, K.L., Taylor, A., Thomas, N., Kleim, J., Sibson, N.R., Bannerman, D., Johansen-Berg, H., 2013. Motor Skill Learning Induces Changes in White Matter Microstructure and Myelination.
Sano, H., Nagai, Y., Miyakawa, T., Shigemoto, R., Yokoi, M., 2008. Increased social interaction in mice deficient of the striatal medium spiny neuron-specific phosphodiesterase 10A2. J. Neurochem. 105 (2), 546–556.
Shibata, S., Murota, Y., Nishimoto, Y., Yoshimura, M., Nagai, T., Okano, H., Siomi, M.C., 2015. Immuno-electron microscopy and electron microscopic in situ hybridization for visualizing piRNA biogenesis bodies in Drosophila ovaries. Methods Mol. Biol. 1328, 163–178.
Shih, Y.Y., Chen, C.C., Shyu, B.C., Lin, Z.J., Chiang, Y.C., Jaw, F.S., Chen, Y.Y., Chang, C., 2009. A new scenario for negative functional magnetic resonance imaging signals: endogenous neurotransmission. J. Neurosci. 29 (10), 3036–3044.
Shih, Y.Y., Huang, S., Chen, Y.Y., Lai, H.Y., Kao, Y.C., Du, F., Hui, E.S., Duong, T.Q., 2014. Imaging neurovascular function and functional recovery after stroke in the rat striatum using forepaw stimulation. J. Cerebr. Blood Flow Metabol. 34 (9), 1483–1492.
Tanaka, K.F., Matsui, K., Sasaki, T., Sano, H., Sugio, S., Fan, K., Hen, R., Nakai, J., Yanagawa, Y., Hasuwa, H., Okabe, M., Deisseroth, K., Ikenaka, K., Yamanaka, A., 2012. Expanding the repertoire of optogenetically targeted cells with an enhanced gene expression system. Cell Rep. 2 (2), 397–406.
Thomason, M.E., Thompson, P.M., 2011. Diffusion imaging, white matter, and psychopathology. Annu. Rev. Clin. Psychol. 7, 63–85.
Veldsman, M., Cumming, T., Brodtmann, A., 2015. Beyond BOLD: optimizing functional imaging in stroke populations. Hum. Brain Mapp. 36 (4), 1620–1636.
Waxman, S.G., 1980. Determinants of conduction velocity in myelinated nerve fibers. Muscle Nerve 3 (2), 141–150.
Wichmann, T., Dostrovsky, J.O., 2011. Pathological basal ganglia activity in movement disorders. Neuroscience 198, 232–244.
Wiegert, J.S., Oertner, T.G., 2013. Long-term depression triggers the selective elimination of weakly integrated synapses. Proc. Natl. Acad. Sci. U. S. A 110 (47), E4510–E4519.
Yano, R., Hata, J., Abe, Y., Seki, F., Yoshida, K., Komaki, Y., Okano, H., Tanaka, K.F., 2018. Quantitative temporal changes in DTI values coupled with histological properties in cuprizone-induced demyelination and remyelination. Neurochem. Int. S0197–0186 (17), 30350–30359.
Zerbi, V., Kleinnijenhuis, M., Fang, X., Jansen, D., Veltien, A., Van Asten, J., Timmer, N., Dederen, P.J., Kiliaan, A.J., Heerschap, A., 2013. Gray and white matter degeneration revealed by diffusion in an Alzheimer mouse model. Neurobiol. Aging 34 (5), 1440–1450.
Zhou, Q., Homma, K.J., Poo, M.M., 2004. Shrinkage of dendritic spines associated with long-term depression of hippocampal synapses. Neuron 44 (5), 749–757.